Quantitative Analysis of the Reduction Kinetics Responsible for the One-Pot Synthesis of Pd−Pt Bimetallic Nanocrystals with Different Structures

Ming Zhou,[†,‡] Helan Wang,[†] Madeline Vara,[§] Zachary D. Hood,[§,∥] Ming Luo,[†] Tung-Han Yang,[†] Shixiong Bao,[†] Miaofang Chi,[∥] Peng Xiao,[‡] Yunhuai Zhang,[‡] and Younan Xia*,[†,§]

[†]The Wallace H. Coulter Department of Biomedical Engineering, Georgia Institute of Technology and Emory University, Atlanta, Georgia 30332, United States

[‡]College of Chemistry and Chemical Engineering, Chongqing University, Chongqing 400044, China

[§]School of Chemistry and Biochemistry, Georgia Institute of Technology, Atlanta, Georgia 30332, United States

[∥]Center for Nanophase Materials Sciences, Oak Ridge National Laboratory, Oak Ridge, Tennessee 37831, United States

S *Supporting Information*

ABSTRACT: We report a quantitative understanding of the reduction kinetics responsible for the formation of Pd−Pt bimetallic nanocrystals with two distinctive structures. The syntheses involve the use of KBr to manipulate the reaction kinetics by influencing the redox potentials of metal precursor ions via ligand exchange. In the absence of KBr, the ratio between the initial reduction rates of $PdCl_4^{2-}$ and $PtCl_4^{2-}$ was about 10.0, leading to the formation of Pd@Pt octahedra with a core−shell structure. In the presence of 63 mM KBr, the products became Pd−Pt alloy nanocrystals. In this case, the ratio between the initial

reduction rates of the two precursors dropped to 2.4 because of ligand exchange and, thus, the formation of $PdBr_4^{2-}$ and $PtBr_4^{2-}$. The alloy nanocrystals took a cubic shape owing to the selective capping effect of Br^- ions toward the {100} facets. Relative to the alloy nanocubes, the Pd@Pt core−shell octahedra showed substantial enhancement in both catalytic activity and durability toward the oxygen reduction reaction (ORR). Specifically, the specific (1.51 mA cm^{-2}) and mass (1.05 A mg^{-1} $_{Pt}$) activities of the core−shell octahedra were enhanced by about four- and three-fold relative to the alloy nanocubes (0.39 mA cm^{-2} and 0.34 A mg^{-1} $_{Pt}$, respectively). Even after 20000 cycles of accelerated durability test, the core−shell octahedra still exhibited a mass activity of 0.68 A mg^{-1} $_{Pt}$, twice that of a pristine commercial Pt/C catalyst.
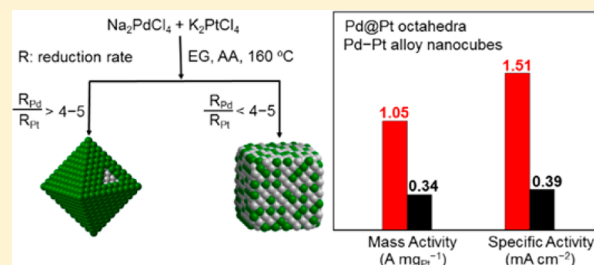
INTRODUCTION

The composition of noble-metal nanocrystals can be manipulated to tailor their properties for a range of applications, including those related to catalysis, plasmonics, and medicine.[1−5] To this end, bimetallic nanocrystals consisting of two distinct metals have received great interest, as they typically exhibit not only a combination of the properties associated with individual metals but also enhancement or synergy arising from the electronic coupling between the two metals.[6,7] Bimetallic nanocrystals can take, at least, two different types of structures: core−shell and alloy.[8,9] While alloy nanocrystals are typically produced through the co-reduction of two metal precursors in one pot,[10,11] core−shell nanocrystals are commonly prepared using seed-mediated growth.[12−14] As a hallmark, homogeneous nucleation and growth can be disentangled from each other in seed-mediated growth to allow for optimization of the experimental conditions separately.[12,15−18] Despite its versatility and great control over the final products, seed-mediated growth is less attractive than a one-pot approach when one has to consider issues related to

the volume, time, and cost of a production process. As a result, the one-pot route has received considerable interest in recent years due to its potential for easy scaling-up with a goal toward high-volume production.[19−24] The major challenge in one-pot synthesis is to elucidate the growth pathways that lead to the formation of bimetallic nanocrystals with distinct structures by quantitatively correlating the outcome of a synthesis with a specific experimental parameter.

With Pd−Pt nanocrystals as a typical example, here we demonstrate that their structures can be predicted by quantitatively knowing the reduction kinetics of the Pd(II) and Pt(II) precursors. Specifically, we measured the reduction rates of $PdCl_4^{2-}$ and $PtCl_4^{2-}$ precursors in the absence and presence of Br^- ions, and correlated the kinetic data with the structures observed for the bimetallic nanocrystals. When the synthesis was conducted in the absence of Br^- ions, we obtained Pd@Pt core−shell octahedra because of the large

difference between the initial reduction rates of $PdCl_4^{2-}$ and $PtCl_4^{2-}$. When conducted in the presence of 42 mM and 63 mM Br^- ions, the products were switched to Pd–Pt alloy nanocrystals because the initial reduction rates of two precursors became comparable to each other due to the formation of $PdBr_4^{2-}$ and $PtBr_4^{2-}$ through ligand exchange. The presence of Br^- ions at an adequate concentration also led to the formation of nanocrystals with a cubic shape due to their selective capping effect toward the {100} facets. Such a quantitative understanding would offer mechanistic insights into the rational design and synthesis of bi- and even multimetallic nanocrystals with well-controlled structures and properties.

It should be pointed out that one-pot synthesis involving the co-reduction of two different metal precursors has been reported in the literature.[11,25−33] Most of those studies involved the formation of alloy nanoparticles or nanocrystals, with a very small number of them reporting the formation of core−shell nanocrystals. Specifically, Han and co-workers demonstrated the synthesis of Au@Pd core−shell nanocrystals by co-reducing $HAuCl_4$ and K_2PdCl_4 in an aqueous solution, with the use of cetyltrimethylammonium chloride (CTAC) as both a reductant and a stabilizer.[30] Li and co-workers reported the synthesis of Au@Co core−shell nanocrystals by co-reducing $HAuCl_4$ and $Co(NO_3)_2$ in octadecylamine.[31] Yamauchi and co-workers demonstrated the synthesis of Au@Pd@Pt triple-layered core−shell nanocrystals using $HAuCl_4$, Na_2PdCl_4, and K_2PtCl_4 as the precursors and ascorbic acid as a reducing agent in an aqueous system.[32] Skrabalak and co-workers systematically studied the co-reduction of $Pd(acac)_2$ and three Pt precursors with different ligands in oleylamine and demonstrated the synthesis of Pd@Pt core−shell dendritic bundles and Pd−Pt alloy nanodendrites.[33] Despite these demonstrations, it should be pointed out that all these studies were largely based on a trial-and-error approach to the optimization of the experimental parameters due to the lack of a quantitative understanding of the reduction kinetics involved in the synthesis. The work presented in this paper demonstrates that the initial reduction rates of metal precursors can serve as a quantitative knob for manipulating and, more significantly, predicting the structure to be taken by a bimetallic nanocrystal.

■ EXPERIMENTAL SECTION

Chemicals and Materials. Ethylene glycol (EG, lot no. L05B13) was purchased from J. T. Baker. Sodium tetrachloropalladate(II) (Na_2PdCl_4, 99.99%), potassium tetrachloroplatinate(II) (K_2PtCl_4, 99.99%), potassium bromide (KBr), poly(vinylpyrrolidone) (PVP, M.W. ≈ 55000), L-ascorbic acid (AA), hydrochloric acid (HCl, 37%), acetic acid (99.7%), perchloric acid ($HClO_4$, 70%, PPT grade, Veritas), and ethanol (Pharmco Products, 200 proof) were all obtained from Sigma-Aldrich. We used all the chemicals as received and prepared all aqueous solutions using deionized (DI) water with a resistivity of 18.2 MΩ cm.

Synthesis of Pd−Pt Bimetallic Nanocrystals. We could selectively obtain Pd−Pt bimetallic nanocrystals with distinctive structures and shapes using the same procedure, except for the use of KBr to manipulate the reduction rates of the two metal precursors. In particular, Pd@Pt core−shell octahedra were obtained by injecting a mixture of Na_2PdCl_4 and K_2PtCl_4 (in EG) into another EG solution containing PVP and AA with a pipet. In a standard synthesis, 50 mg of PVP, 50 mg of AA, and 7.0 mL of EG were mixed in a vial at room temperature (22 °C) under magnetic stirring for 10 min. Subsequently, 3 mL of EG solution containing 38.2 mg of Na_2PdCl_4 and 14.6 mg of K_2PtCl_4 was added with a pipet, and the mixture was kept under stirring for another 10 min at room temperature. The

mixture was then heated in an oil bath held at 160 °C for 1 h, followed by natural cooling to room temperature. The product was collected by centrifugation at 55000 rpm, washed once with acetone and twice with DI water, and finally redispersed in 10 mL of water. The number of Pt atomic layers could be controlled by simply adjusting the amount of Pt precursor introduced into the reaction solution. For the synthesis of Pd−Pt alloy nanocubes, the protocol was essentially the same as the procedure used for the standard synthesis of Pd@Pt core−shell octahedra, except for the addition of 75 mg of KBr.

Etching of Pd from the Pd@Pt Core−Shell Octahedra. In a typical procedure, we mixed 300 mg of KBr, 50 mg of PVP, 30 mg of $FeCl_3$, 0.18 mL of HCl, and 5.0 mL of water in a glass vial. The mixture was held at 80 °C in an oil bath under magnetic stirring, and then 0.25 mL of an aqueous suspension of the Pd@Pt core−shell octahedra was introduced. After etching for 1 or 1.5 h, the solid product was collected by centrifugation at 55000 rpm, followed by washing five times with ethanol and DI water.

Quantitative Analysis of the Reaction Rates Corresponding to the Formation of Pd−Pt Bimetallic Nanocrystals with Distinctive Structures. We measured the reduction rates of the Pd and Pt precursors by analyzing the concentrations of Pd(II) and Pt(II) ions remaining in the reaction solution at different time points using inductively coupled plasma mass spectrometry (ICP-MS, NexION 300Q, PerkinElmer).[34,35] In a standard procedure, the timer would start running as soon as the reagents were mixed in a vial immersed in an oil bath held at 160 °C. An aliquot of 0.2 mL was sampled from the reaction solution at different time points using a glass pipet and immediately injected into 0.8 mL of aqueous KBr solution (500 mg mL^{-1}) held in an ice bath to quickly quench the reaction. As demonstrated in our early work,[34,35] the quick drop in temperature and the presence of excess Br^- ions would quench the reaction and thus preserve the concentration of the precursor ions. The solution was centrifuged at 55000 rpm for 60 min to precipitate out all the metal nanocrystals, leaving behind Pd(II) and Pt(II) ions in the supernatant. The supernatant was then collected and further diluted with 1% (v/v) aqueous HNO_3 solution to a level of 100 ppb for ICP-MS analysis. Even though there was a time gap between the isolation of remaining precursor ions and their analysis via the workup procedure, the reduction of the Pd and Pt species during this period of time should be negligible due to the formation of more stable $PdBr_4^{2-}$ and $PtBr_4^{2-}$ via ligand exchange. The concentrations of Pd(II) or Pt(II) ions obtained at different time points were then used to determine the rate constant (k) by performing a linear fit to the plot of $\ln[Pd(II)]$ or $\ln[Pt(II)]$ vs reaction time, with the slope of the regression line taken as $-k$. When the temperature is fixed, the rate constant can be used to calculate the instantaneous concentrations of remaining Pd(II) or Pt(II) ions as a function of reaction time for all the syntheses conducted in the present work.

Instrumentation. Transmission electron microscopy (TEM) images were taken using a Hitachi HT7700 (Hitachi, Tokyo, Japan) operated at 120 kV. The samples were prepared by drop casting the nanocrystal dispersions on carbon-coated Cu grids and drying under ambient conditions. High-resolution high-angle annular dark-field scanning transmission electron microscopy (HAADF-STEM) and tomography images were taken on a JEOL JEM 2200FS STEM/TEM microscope equipped with a CEOS probe corrector (Heidelberg, Germany) to provide a nominal image resolution of 0.07 nm. EDX analysis was performed in STEM mode using an aberration-corrected JEOL 2200FS electron microscope equipped with a Bruker-AXS SDD detector. The metal contents were measured using ICP-MS.

Preparation of the Working Electrodes. First, the Pd@Pt core−shell octahedra or Pd−Pt alloy nanocubes were loaded onto a carbon support (Ketjen Black EC-300J) with a metal content of 20% based on the total mass of Pd and Pt (determined by ICP-MS). Typically, 2 mg of the bimetallic nanocrystals and 8 mg of Ketjen black were mixed in 8 mL of ethanol under continuous ultrasonication for 4 h. The carbon-supported Pd−Pt nanocrystals were then collected by centrifugation, redispersed in 10 mL of acetic acid, and heated at 60 °C for 10 h to help clean the surface of the nanocrystals. The final catalyst was collected by centrifugation, followed by washing six times with

ethanol. After drying, 3 mg of the catalyst was redispersed in a mixture of 1 mL of water, 1 mL of isopropanol, and 40 μL of 5% Nafion under ultrasonication for 60 min. Finally, 10 μL of the suspension was placed on a precleaned glassy carbon rotating disk electrode (RDE) from Pine Research Instrumentation (0.196 cm^2 in geometric area) and dried under ambient conditions at room temperature.

Electrochemical Measurements. We conducted electrochemical measurements using a CHI 600E potentiostat (CH Instruments), with a hydroflex hydrogen reference electrode (Gaskatel) and a Pt mesh serving as the reference and counter electrodes, respectively. All potentials were presented with reference to the reversible hydrogen electrode (RHE), or V_{RHE}. The electrolyte was prepared by diluting a 70% stock solution with DI water to 0.1 M HClO$_4$. The CV curve was recorded at room temperature in a N$_2$-saturated 0.1 M HClO$_4$ solution in the potential range of 0.08–1.1 V_{RHE} at a scanning rate of 50 mV s^{-1}. We calculated the specific electrochemical active surface area (ECSA) of each catalyst on the basis of the average charges associated with hydrogen adsorption and desorption in the region of 0.08–0.43 V_{RHE} with a reference value of 210 μC cm^{-2} (for Pd–Pt alloy nanocubes) or 240 μC cm^{-2} (for Pd@Pt core–shell octahedra) for the desorption of a monolayer of hydrogen from the Pt surface. We measured the ORR activities of catalysts at room temperature in the potential range of 0.08–1.1 V_{RHE} in an O$_2$-saturated 0.1 M HClO$_4$ solution using the RDE method at a scanning rate of 10 mV s^{-1} and a rotating speed of 1600 rpm. The ORR data were corrected by ohmic *iR* drop compensation. For the accelerated durability test, we recorded CVs and ORR polarization curves after sweeping the potential in the range of 0.6 and 1.1 V_{RHE} for 5000, 10000, 15000, and 20000 cycles at a rate of 0.1 V s^{-1} in an O$_2$-saturated 0.1 M HClO$_4$ solution at room temperature.

RESULTS AND DISCUSSION

Synthesis and Characterization of Pd–Pt Bimetallic Nanocrystals. In the current system, the structure taken by the nanocrystals was found to be largely determined by the amount of KBr added into the reaction solution when all other experimental parameters, including temperature, reductant, solvent, and the concentrations of precursors, were kept the same. If no KBr was added, we obtained Pd@Pt core–shell octahedra. In contrast, the products changed to alloy nanocubes when 42 mM or 63 mM KBr was added. Our mechanistic study clearly indicates that a correlation exists between the structure of the Pd–Pt bimetallic nanocrystals and the relative initial reduction rates of the Pd and Pt precursors involved.

Figure 1A schematically illustrates how Pd@Pt core–shell octahedra and Pd–Pt alloy nanocubes are formed in the absence and presence of KBr, respectively. As expected, KBr can influence the redox potentials of given metal ions because of ligand exchange. In the absence of KBr, when the EG solution containing Na$_2$PdCl$_4$, K$_2$PtCl$_4$, AA, and PVP was heated to 160 °C, it turned black immediately, implying the formation of metal nanocrystals due to the fast reduction by AA and EG. As shown by the TEM image in Figure 1B for a sample collected at a reaction time of 1 h, we obtained Pd@Pt core–shell octahedra enclosed by {111} facets, together with an average edge length of 6.3 ± 1.1 nm. In this case, the standard reduction potential (E^0) of PdCl$_4^{2-}$/Pd (0.62 V vs RHE) is more negative than that of PtCl$_4^{2-}$/Pt (0.74 V vs RHE) when they are dissolved in the same medium.[36] As such, PdCl$_4^{2-}$ should be reduced first, followed by PtCl$_4^{2-}$. In contrast, Pd–Pt alloy nanocubes enclosed by {100} facets were obtained under the same conditions, except for the introduction of 63 mM KBr (Figure 1C). The average edge length of the Pd–Pt alloy nanocubes was 6.1 ± 0.9 nm. These results indicate that Pd–Pt bimetallic nanocrystals with different structures and shapes could be deterministically obtained through a one-pot route by
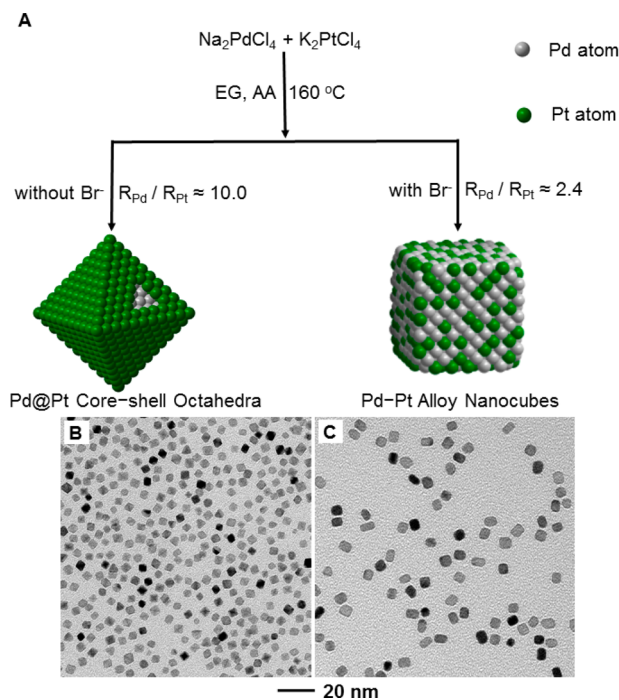

Figure 1. (A) Schematic illustration describing the major differences involved in the formation of Pd–Pt bimetallic nanocrystals in the absence and presence of Br⁻ ions, respectively. (B, C) TEM images of the Pd–Pt core–shell octahedra and Pd–Pt alloy nanocubes, respectively.

manipulating the amount of KBr involved while all other experimental conditions were fixed.

Figure 2A shows a low-magnification HAADF-STEM image of the Pd@Pt core–shell octahedra. The HAADF-STEM image taken from an individual octahedron is shown in Figure 2B, revealing the {111} facets on the side faces and the {100} facets at the truncated corners. The contrast between the Pt shell (brighter) and the Pd core can be attributed to the large difference in atomic number between these two elements. The image suggests that the Pt shell was about two atomic layers in thickness. We also determined the average number of Pt atomic layers by ICP-MS and obtained a value of 1.9. As the number of Pt atomic layers derived from the ICP-MS analysis represents the average value from a large number of nanoparticles, it is used exclusively in our discussion unless otherwise specified. We further analyzed the octahedral nanocrystals by energy-dispersive X-ray spectroscopy (EDX) mapping to confirm the formation of a Pd@Pt core–shell structure (Figure 2C). From the ICP-MS data (Table S1), the Pd/Pt molar ratio for the Pd@Pt core–shell octahedra was 3.73, almost identical to the value of 3.70 derived for the feeding molar ratio between the Pd and Pt precursors. This result is reasonable because the conversion of Pd and Pt precursors could reach a level of >99% in a polyol synthesis. The energy-dispersive X-ray spectroscopy (EDS) line scans across an octahedron confirm that the Pd and Pt elements were only detected from the core and shell regions, respectively, of the octahedral nanocrystal (Figure 2D). To further confirm the core–shell structure, we also tried to etch away the Pd cores from the Pd@Pt octahedra in an effort to obtain Pt nanocages. In this case, it was noted that the Pt nanocages derived from the Pd@Pt$_{1.9L}$ octahedra tended to be fragmented because of the relatively weak mechanical strength associated with the ultrathin walls when the standard etching
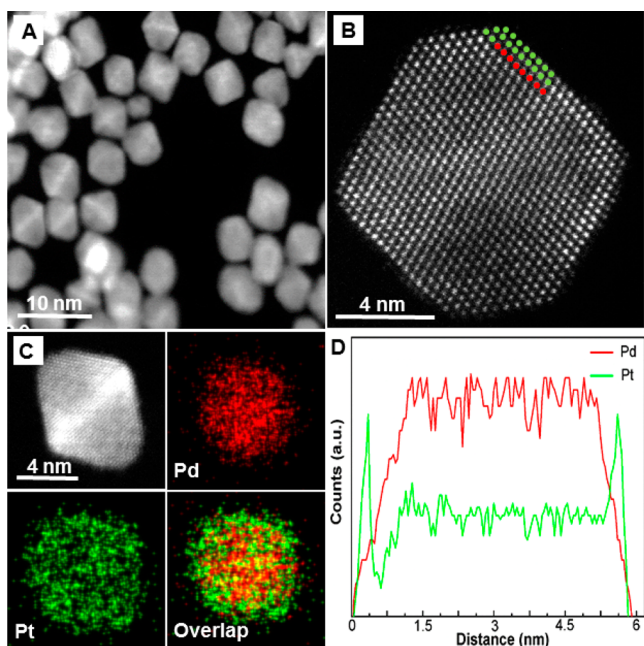
Figure 2. (A) Low-magnification HAADF-STEM image of the Pd@Pt octahedra. (B) Atomic-resolution HAADF-STEM image taken from a single Pd@Pt octahedron, revealing the detailed arrangements of Pd and Pt atoms (red dots: Pd atoms; green dots: Pt atoms). (C) HAADF-STEM image of a Pd@Pt octahedron and the corresponding EDX mapping of Pd and Pt. (D) EDS line scans of Pd and Pt recorded from a Pd@Pt octahedron.

Figure 3. (A) Low-magnification HAADF-STEM images of two Pd−Pt alloy nanocubes. (B) Atomic-resolution HAADF-STEM image taken from a single Pd−Pt alloy nanocube. (C) HAADF-STEM image of two Pd−Pt alloy nanocubes and the corresponding EDX mapping of Pd and Pt. (D) EDS line scan recorded from a Pd−Pt alloy nanocube.

procedure was used. To address this issue, we increased the amount of $PdCl_4^{2-}$ from 14.6 mg to 29.0 mg. We obtained Pd@Pt$_{2.9L}$ octahedra, which could be transformed into Pt-based octahedral nanocages by selectively removing the Pd cores (Figure S1), confirming that the original octahedra indeed had a core−shell structure.

We also characterized the Pd−Pt alloy nanocubes by HAADF-STEM. The images in Figure 3A and B were taken from the nanocrystals, with their {100} facets on the side faces clearly revealed. The continuous lattice extending across the entire surface in the same orientation suggests that the nanocubes had a single-crystal structure. The lattice spacing along the edge of a nanocube was 0.19 nm, in agreement with the {200} lattice spacing of the face-centered cubic (*fcc*) Pd or Pt,[37] further confirming that the Pd−Pt alloy nanocubes were bounded by {100} facets. Elemental mapping based on EDS confirmed that the nanocubes were composed of a Pd−Pt alloy (Figure 3C). Figure 3D shows line-scan EDX profiles of Pd and Pt elements recorded through the center of an individual nanocube, indicating that both the Pd and Pt atoms were well-distributed throughout the nanocrystal. The same crystal structure and negligible lattice mismatch between Pd and Pt (0.77%) were critical to the formation of a single-crystal, alloy structure.[14,18] According to the data obtained from ICP-MS (Table S1), the conversions of Pd and Pt precursors dropped to 87% in the presence of KBr, indicating that the presence of Br− ions would decelerate the reduction of both the Pd and Pt precursors.

Mechanistic Investigation of the Formation of Bimetallic Nanocrystals with Distinctive Structures. To quantitatively understand the effect of reaction kinetics on the transition from a core−shell to an alloy structure, it is necessary to know the reduction rates for both metal precursors by
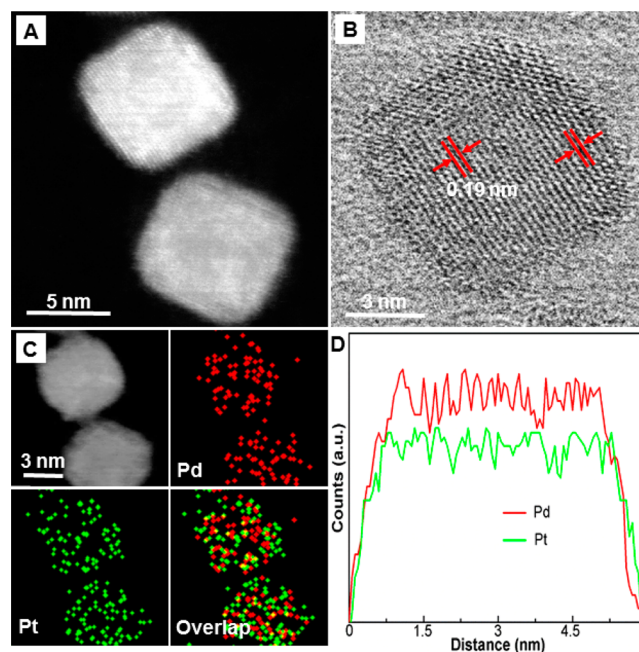
deriving the concentrations of precursor ions remaining in the reaction solution at different time points. Due to the involvement of collision and electron transfer between precursor ion and reductant molecule, the reduction of metal precursors generally follows a second-order rate law. As such, the reduction rate is expected to be directly proportional to the concentrations of both reagents.[38] Here we employed a pseudo-first-order rate law by supplying the reductants (AA and EG in the present work) in great excess relative to the precursor ($PdCl_4^{2-}$ or $PtCl_4^{2-}$), and thus, the concentrations of reductants should remain essentially the same during the entire synthesis. The presence of reductants in large excess not only ensures a pseudo-first-order rate but also enables complete reduction of the precursors ions into atoms. For a pseudo-first-order reaction of A + B → product, the rate involved can be expressed as

$$\text{rate} = k'[A][B] = k[A] = -\frac{d[A]}{dt} \qquad (1)$$

where k is the combined rate constant; and [A] and [B] are the instantaneous concentrations of the precursor and reductant. The combined rate constant is determined by a combination of multiple experimental parameters, including the types of reductant and solvent, as well as the reaction temperature. It should be pointed out that the pseudo-first-order rate law is still valid when more than one reductant (e.g., AA and EG in the present work) is involved, as long as they are all in large excess relative to the precursor.

Equation 1 can be easily integrated to obtain

$$\ln[A]_t = -kt + \ln[A]_0 \qquad (2)$$

where $[A]_0$ and $[A]_t$ correspond to the molar concentrations of the precursor at the beginning of a synthesis and at a specific
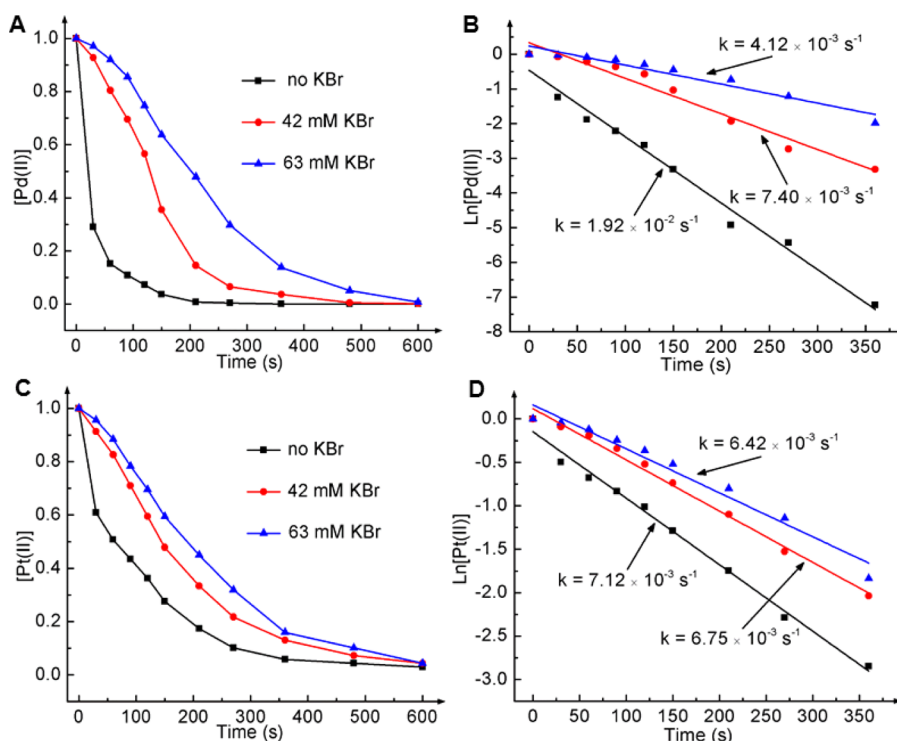
Figure 4. Quantitative analysis of the reduction kinetics involved in the synthesis of the Pd−Pt bimetallic nanocrystals. (A, C) Plots showing the concentrations of Pd(II) and Pt(II) ions remaining in the solutions as a function of reaction time in the absence (black curves) and presence (red curves and blue curves) of KBr, respectively. (B, D) Plots of $\ln[Pd(II)]$ and $\ln[Pt(II)]$ as a function of reaction time, giving straight lines with slopes corresponding to the rate constants, respectively. Note that the concentrations used in the plots were normalized to the initial concentration.

time of t, respectively. In this case, a straight line can be obtained with a slope of $-k$ by plotting $\ln[A]_t$ as a function of reaction time. In a typical measurement, 0.2 mL of aliquot was sampled from the reaction solution using a glass pipet at each time point and immediately injected into a highly concentrated KBr solution held in an ice bath. The quick drop in temperature and the presence of excess Br$^-$ ions could effectively quench the reduction reaction and thus preserve the concentration of precursor ions. It should be pointed out that the extraction of solution from a reaction system to a certain extent should not affect the reduction kinetics because the reduction rate is determined by the concentrations of the reactants rather than their amounts or the volume of the reaction solution. We added an excess amount of KBr to ensure that the Pd(II) and Pt(II) ions would essentially exist in the form of $PdBr_4^{2-}$ and $PtBr_4^{2-}$ through a complete ligand exchange due to the much higher stability of $PdBr_4^{2-}$ and $PtBr_4^{2-}$.[39,40] The highly concentrated KBr solution played a critical role in preventing the precursor ions from being further reduced once sampled from the reaction solution.

As shown in Figure 4A, 92.8% of the $PdCl_4^{2-}$ was reduced to Pd atoms within 2 min in the absence of KBr, and this value increased to 99.9% at $t = 10$ min. In comparison, the conversion of $PtCl_4^{2-}$ to Pt atoms was only 61.8% within the first 2 min, suggesting that $PtCl_4^{2-}$ was reduced at a much slower rate than $PdCl_4^{2-}$ under the same conditions, particularly in the early stage of a synthesis (Figure 4C). Figure 4B and D shows plots of $\ln[PdCl_4^{2-}]_t$ and $\ln[PtCl_4^{2-}]_t$ as a function of reaction time, respectively. It can be seen that the values of $\ln[PdCl_4^{2-}]_t$ or $\ln[PtCl_4^{2-}]_t$ indeed decrease linearly with reaction time, demonstrating that the reduction was first-order with respect to the metal precursor concentration. In addition, it is

reasonable to assume that no autocatalytic reduction was involved for the synthesis described here because the values of $\ln[PdCl_4^{2-}]_t$ and $\ln[PtCl_4^{2-}]_t$ did not show any abrupt changes deviating from the linear plot. From the slopes of the linear regression lines, the rate constants were determined to be 1.92 $\times$ 10^{-2} and 7.12 $\times$ 10^{-3} s^{-1} for the reduction of $PdCl_4^{2-}$ and $PtCl_4^{2-}$, respectively, at 160 °C. The ratio of rate constants between $PdCl_4^{2-}$ and $PtCl_4^{2-}$ was about 2.7. Combined with the initial concentration of $PdCl_4^{2-}$ (1.3 $\times$ 10^{-2} M) and $PtCl_4^{2-}$ (3.5 $\times$ 10^{-3} M), the corresponding initial reduction rates were 2.50 $\times$ 10^{-4} and 2.49 $\times$ 10^{-5} M s^{-1}, differing by about 10-fold. It is worth pointing out that the concentration of the Pt precursor was almost doubled for the synthesis of $Pd@Pt_{2.9L}$ octahedra relative to $Pd@Pt_{1.9L}$ octahedra. As confirmed by the results shown in Figure S1, a core−shell structure was still formed even though the ratio of initial reduction rates between $PdCl_4^{2-}$ and $PtCl_4^{2-}$ was reduced from 10 to 5.

We further extended the kinetic measurements to the synthesis in the presence of 63 mM KBr. As shown in Figure 4A and C, the presence of Br$^-$ ions would simultaneously decelerate the conversion of precursor ions to atoms. Only 25.4% of the Pd(II) precursor was reduced to Pd atoms within 2 min, implying a significant drop in reduction rate for the Pd precursor when 63 mM KBr was added. In contrast, the conversion of Pt(II) precursor to Pt atoms decreased from 61.8% to 30.4% within the first 2 min. It has been shown that Br$^-$ ions had a significant impact on the reaction kinetics, further suggesting the stronger binding strength of Br$^-$ to Pd^{2+} and Pt^{2+} ions than Cl$^-$.[40] These results indicate that the ligand exchange between Br$^-$ and Cl$^-$ could be completed within a very short period of time once they are mixed. We conducted a set of experiments to confirm the ligand exchange process by
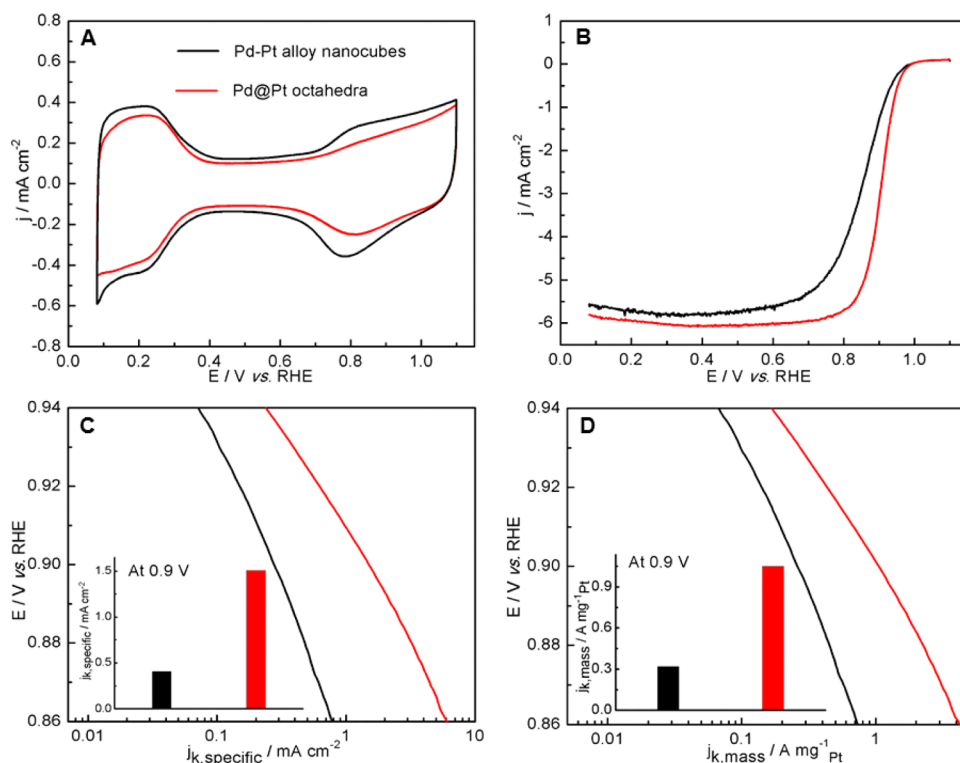
Figure 5. Electrocatalytic properties of the Pd@Pt octahedra and Pd−Pt alloy nanocubes for the oxygen reduction reaction. (A) Cyclic voltammetry curves of the Pd@Pt octahedra and Pd−Pt alloy nanocubes (both on carbon support) in N_2-saturated 0.1 M $HClO_4$ solutions. The scanning rate was 50 mV s^{-1}. (B) Comparison of the positive-going ORR polarization curves of the catalysts in O_2-saturated 0.1 M $HClO_4$ solutions. The scanning rate was 10 mV s^{-1}, and the rotation speed was 1600 rpm. The currents were normalized to the geometric area of the rotating disk electrode (0.196 cm^2). (C, D) Specific and mass ORR activities given as kinetic current densities (j_k) normalized to the ECSAs and Pt masses of the catalysts, respectively.

recording UV−vis spectra from an aqueous $PdCl_4^{2-}$ solution after the introduction of KBr up to 63 mM. As shown in Figure S2A, the presence of KBr at a molar concentration of 63 mM was able to convert all the $PdCl_4^{2-}$ to $PdBr_4^{2-}$. We also compared the UV−vis spectra of the reaction solution containing both the Pd and Pt precursors in the absence and presence of 63 mM KBr, respectively. Again, the absorption peak shift in Figure S2B confirms that ligand exchange occurred after the introduction of KBr. Most significantly, the gap between the reduction rates of the Pd and Pt precursors could be markedly narrowed by adding 63 mM KBr. On the basis of the plots shown in Figure 4B and D, the rate constants became 4.12×10^{-3} and 6.42×10^{-3} s^{-1} for the Pd and Pt precursors, respectively, in the presence of 63 mM KBr. In the case of Pd, we conducted the reduction reaction three times and measured the reduction rate constants. We obtained 4.12×10^{-3}, 4.10×10^{-3}, and 4.13×10^{-3} s^{-1} for the rate constant, which gave a standard deviation of 1.58×10^{-5}. This set of data indicates that the measurements are reasonably accurate. The ratio of the rate constants between Pd and Pt precursors dropped to 0.6. Combined with the initial concentrations of Pd(II) (1.3×10^{-2} M) and Pt(II) (3.5×10^{-3} M), their initial reduction rates became comparable to each other: 5.36×10^{-5} versus 2.25×10^{-5} M s^{-1}, with a ratio of 2.4. The smaller difference in reduction rates resulted in the formation of an alloy structure.

When the concentration of KBr was reduced from 63 mM to 42 mM, the rate constants became 7.40×10^{-3} and 6.75×10^{-3} s^{-1} for the Pd and Pt precursors, respectively. As shown in Figure S3A, most of the nanocrystals could still be obtained with a cubic shape. To identify the structure of these bimetallic nanocrystals, we subjected the sample to Pd etching. The TEM

image in Figure S3B indicates that these nanocrystals had an alloy rather than core−shell structure. In this case, the initial reduction rates of the Pd and Pt precursors were 9.62×10^{-5} and 2.36×10^{-5}, with a ratio of about 4.1. When combined with the kinetic data involved in the synthesis shown in Figure S1, it can be concluded that the structure will take a transition from alloy to core−shell when the initial reduction rate of the Pd precursor is about 4−5-fold greater than that of the Pt precursor. Taken together, these results quantitatively indicate that the structure developed in the products was determined by the reaction kinetics, which could be conveniently manipulated through the addition of KBr. The presence of Br$^-$ ions in the reaction solution also resulted in the formation of nanocrystals with a cubic shape, owing to the selective capping effect of Br$^-$ ions toward the {100} facets.

Electrochemical Measurements. We also evaluated the catalytic activities of the Pd@Pt core−shell octahedra and Pd−Pt alloy nanocubes toward ORR. Prior to electrochemical measurements, the bimetallic nanocrystals were dispersed on carbon to obtain Pd@Pt/C and Pd−Pt alloy/C catalysts. Figure 5A shows cyclic voltammograms (CVs) recorded from the two different types of catalysts in the potential range of 0.08−1.1 V. The ECSAs of the catalysts were calculated from the average charges associated with hydrogen adsorption and desorption between 0.08 and 0.43 V_{RHE}. The specific ECSAs of the catalysts were obtained by normalizing against the Pt mass, and the values were 70.0 and 88.5 m^2 g^{-1}$_{Pt}$, respectively, for the Pd@Pt/C and Pd−Pt alloy/C catalysts (Table 1). These results confirm that the dispersion of Pt atoms could be retained when deposited as ultrathin shells of only a few atomic layers thick.

Table 1. Comparison of the Electrochemically Active Surface Area (ECSA), Specific Activity (SA), and Mass Activity (MA) toward ORR for the Pd@Pt Octahedra and Pd−Pt Alloy Nanocubes (both were supported on carbon)

	ECSA ($m^2 g^{-1}_{Pt}$)	SA at 0.9 V ($mA cm^{-2}$)	MA at 0.9 V ($A mg^{-1}_{Pt}$)
Pd@Pt octahedra	70.0	1.51	1.05
Pd−Pt nanocubes	88.5	0.39	0.34

Figure 5B shows the positive-going ORR polarization curves recorded from the two catalysts. The specific and mass activities ($j_{k,specific}$ and $j_{k,mass}$) were calculated using the Koutecky−Levich equation and then normalized against the ECSA and Pt mass of the catalyst. Relative to the Pd−Pt alloy/C catalyst, the specific and mass activities of the Pd@Pt/C catalyst were greatly enhanced in the potential region of 0.86−0.94 V_{RHE} (Figure 5C and D). At 0.9 V_{RHE}, the mass activity of the Pd@Pt/C catalyst was 1.05 A mg^{-1}_{Pt}, almost 3.1 times as high as that of the Pd−Pt alloy/C catalyst (0.34 A mg^{-1}_{Pt}). In terms of precious metals (both Pd and Pt), the mass activity of the Pd@Pt/C catalyst still showed 3.3-fold enhancement as compared to that of the Pd−Pt alloy/C catalyst (Figure S4). The specific activity (1.51 mA cm^{-2}) of the Pd@Pt/C catalyst at 0.9 V_{RHE} showed a 3.9-fold enhancement relative to that of the Pd−Pt alloy/C catalyst (0.39 mA cm^{-2}). The enhancement in specific activity can be partially attributed to the ligand effect and the strain arising from the lattice mismatch between Pd and Pt.[41−45] When compared to the Pd@Pt$_{2−3L}$/C catalyst in our previous work,[18] the Pd@Pt/C catalyst showed enhancement in both mass activity (by 1.7-fold) and specific activity (by 2.1-fold) due to a much smaller size to ensure that the active sites are present on the surface at a larger proportion.

In addition to the great enhancement in both specific and mass activities, the Pd@Pt/C catalyst also exhibited remarkable durability (Figure 6). After 5000 cycles of accelerated durability tests at room temperature, the specific ECSA of the Pd@Pt/C catalyst dropped less than 1%. Even after 20000 cycles, the specific ECSA of the Pd@Pt/C catalyst only decreased by 28%. Specifically, the mass activity only dropped to 0.88 A mg^{-1}_{Pt} after 5000 cycles of tests, which corresponds to a loss of only 16% relative to the pristine catalyst, to 0.79 A mg^{-1}_{Pt} after 10000 cycles, to 0.74 A mg^{-1}_{Pt} after 15000 cycles, and to 0.68 A mg^{-1}_{Pt} after 20000 cycles. This value was still more than twice of the pristine activity of a state-of-the-art commercial Pt/C catalyst.[46] Some of the Pd@Pt core−shell octahedra were transformed into spherical nanoparticles with a diameter of 5−6 nm (Figure S5). In comparison with the sample before durability test, the percentage of {111} facets on the surface decreased and the size slightly decreased due to selective dissolution of Pd atoms from the core, leading to the reduced specific and mass activities. These results demonstrate the excellent catalytic durability associated with the core−shell octahedra produced using the one-pot approach.

CONCLUSIONS

In summary, we have quantitatively investigated the role of reduction kinetics in controlling the structures of Pd−Pt bimetallic nanocrystals formed in one-pot syntheses. On the basis of reduction rate constants determined experimentally, we confirmed that Br⁻ ions played a pivotal role in altering the initial reduction rate of the metal precursors and thus the
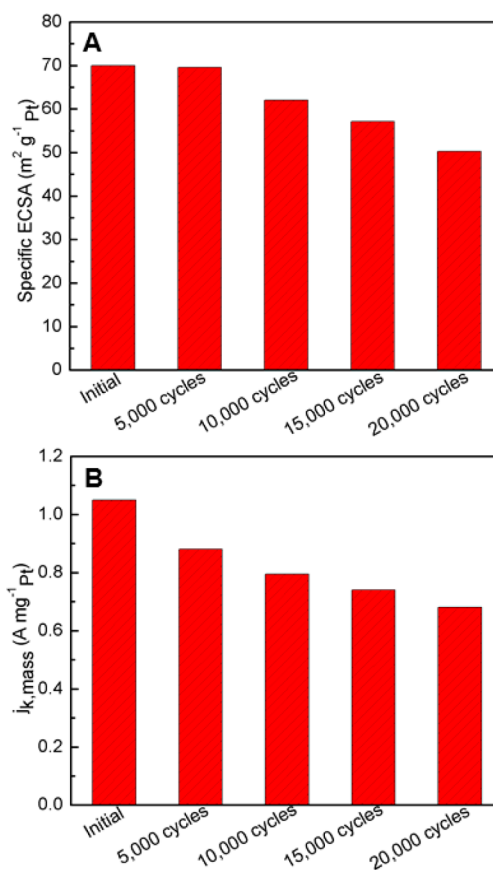

Figure 6. Comparison of (A) the specific ECSAs and (B) mass ORR activities at 0.9 V_{RHE} for the Pd@Pt/C octahedra catalysts before and after the accelerated ORR durability tests.

formation of nanocrystals with distinctive structures. Our analysis suggested that the switching from a core−shell to an alloy structure was determined by the ratio between the initial reduction rates of the two precursors involved. As expected, the Pd@Pt octahedra showed greatly enhanced activity and durability toward ORR when compared to the Pd−Pt alloy nanocubes. After 20000 cycles of accelerated durability test, the Pd@Pt octahedra still showed a mass activity of more than twice the pristine value of a state-of-the-art commercial Pt/C catalyst. This work not only greatly advances our understanding of the nucleation and growth of bimetallic nanocrystals but also paves the way for rational design and deterministic synthesis of noble-metal nanocrystals with desired structures and shapes for catalytic applications.

ASSOCIATED CONTENT

Ⓢ Supporting Information

The Supporting Information is available free of charge on the ACS Publications website at DOI: 10.1021/jacs.6b07213.

TEM images of the Pd@Pt core−shell octahedra and the Pt octahedral nanocages; UV−vis spectra; TEM images of Pd−Pt bimetallic nanocrystals obtained in the presence of 42 mM KBr and the products after Pd etching; mass activities with reference to the total mass of both Pd and Pt; TEM images of the Pd@Pt/C octahedra catalyst before and after the accelerated durability test; a table of the Pd/Pt molar feeding ratios and the Pd/Pt atomic ratios in the particles based on ICP-MS analyses

for both the Pd@Pt core−shell octahedra and Pd−Pt alloy nanocubes (PDF)

■ AUTHOR INFORMATION

Corresponding Author
*younan.xia@bme.gatech.edu

Notes
The authors declare no competing financial interest.

■ ACKNOWLEDGMENTS

■ REFERENCES

(1) Burda, C.; Chen, X.; Narayanan, R.; El-Sayed, M. A. *Chem. Rev.* **2005**, *105*, 1025−1102.
(2) Chen, J.; Lim, B.; Lee, E. P.; Xia, Y. *Nano Today* **2009**, *4*, 81−95.
(3) Sun, Y.; Xia, Y. *Science* **2002**, *298*, 2176−2179.
(4) Rosi, N. L.; Mirkin, C. A. *Chem. Rev.* **2005**, *105*, 1547−1562.
(5) Yavuz, M. S.; Cheng, Y.; Chen, J.; Cobley, C. M.; Zhang, Q.; Rycenga, M.; Xie, J.; Kim, C.; Song, K. H.; Schwartz, A. G.; Wang, L. V.; Xia, Y. *Nat. Mater.* **2009**, *8*, 935−939.
(6) Zhang, H.; Jin, M.; Xia, Y. *Chem. Soc. Rev.* **2012**, *41*, 8035−8049.
(7) Yang, H. *Angew. Chem., Int. Ed.* **2011**, *50*, 2674−2676.
(8) Xie, S.; Choi, S.-I.; Lu, N.; Roling, L. T.; Herron, J. A.; Zhang, L.; Park, J.; Wang, J.; Kim, M. J.; Xie, Z.; Mavrikakis, M.; Xia, Y. *Nano Lett.* **2014**, *14*, 3570−3576.
(9) Cui, C.; Gan, L.; Heggen, M.; Rudi, S.; Strasser, P. *Nat. Mater.* **2013**, *12*, 765−771.
(10) Liu, Y.; Chi, M.; Mazumder, V.; More, K. L.; Soled, S.; Henao, J. D.; Sun, S. *Chem. Mater.* **2011**, *23*, 4199−4203.
(11) Lim, B.; Wang, J.; Camargo, P. H. C.; Cobley, C. M.; Kim, M. J.; Xia, Y. *Angew. Chem., Int. Ed.* **2009**, *48*, 6304−6308.
(12) Lim, B.; Wang, J.; Camargo, P. H. C.; Jiang, M.; Kim, M. J.; Xia, Y. *Nano Lett.* **2008**, *8*, 2535−2540.
(13) DeSantis, C. J.; Peverly, A. A.; Peters, D. G.; Skrabalak, S. E. *Nano Lett.* **2011**, *11*, 2164−2168.
(14) Wang, X.; Choi, S.-I.; Roling, L. T.; Luo, M.; Ma, C.; Zhang, L.; Chi, M.; Liu, J.; Xie, Z.; Herron, J. A.; Mavrikakis, M.; Xia, Y. *Nat. Commun.* **2015**, *6*, 7594.
(15) Habas, S. E.; Lee, H.; Radmilovic, V.; Somorjai, G. A.; Yang, P. *Nat. Mater.* **2007**, *6*, 692−697.
(16) Xia, Y.; Xiong, Y.; Lim, B.; Skrabalak, S. E. *Angew. Chem., Int. Ed.* **2009**, *48*, 60−103.
(17) Xia, Y.; Xia, X.; Peng, H.-C. *J. Am. Chem. Soc.* **2015**, *137*, 7947−7966.
(18) Park, J.; Zhang, L.; Choi, S.-I.; Roling, L. T.; Lu, N.; Herron, J. A.; Xie, S.; Wang, J.; Kim, M. J.; Mavrikakis, M.; Xia, Y. *ACS Nano* **2015**, *9*, 2635−2647.
(19) Choi, S.-I.; Xie, S.; Shao, M.; Odell, J. H.; Lu, N.; Peng, H.-C.; Protsailo, L.; Guerrero, S.; Park, J.; Xia, X.; Wang, J.; Kim, M. J.; Xia, Y. *Nano Lett.* **2013**, *13*, 3420−3425.
(20) Huang, X.; Zheng, N. *J. Am. Chem. Soc.* **2009**, *131*, 4602−4603.
(21) Wu, J.; Qi, L.; You, H.; Gross, A.; Li, J.; Yang, H. *J. Am. Chem. Soc.* **2012**, *134*, 11880−11883.
(22) You, H.; Yang, S.; Ding, B.; Yang, H. *Chem. Soc. Rev.* **2013**, *42*, 2880−2904.
(23) Guo, S.; Li, D.; Zhu, H.; Zhang, S.; Markovic, N. M.; Stamenkovic, V. R.; Sun, S. *Angew. Chem., Int. Ed.* **2013**, *52*, 3465−3468.
(24) Zhang, P.; Dai, X.; Zhang, X.; Chen, Z.; Yang, Y.; Sun, H.; Wang, X.; Wang, H.; Wang, M.; Su, H.; Li, D.; Li, X.; Qin, Y. *Chem. Mater.* **2015**, *27*, 6402−6410.
(25) Huang, X.; Zhang, H.; Guo, C.; Zhou, Z.; Zheng, N. *Angew. Chem.* **2009**, *121*, 4902−4906.
(26) Wang, L.; Nemoto, Y.; Yamauchi, Y. *J. Am. Chem. Soc.* **2011**, *133*, 9674−9677.
(27) Kim, Y.; Noh, Y.; Lim, E. J.; Lee, S.; Choi, S. M.; Kim, W. B. *J. Mater. Chem. A* **2014**, *2*, 6976−6986.
(28) Cui, C.; Gan, L.; Li, H.-H.; Yu, S.-H.; Heggen, M.; Strasser, P. *Nano Lett.* **2012**, *12*, 5885−5889.
(29) Wang, M.; Wang, L.; Li, H.; Du, W.; Khan, M. U.; Zhao, S.; Ma, C.; Li, Z.; Zeng, J. *J. Am. Chem. Soc.* **2015**, *137*, 14027−14030.
(30) Lee, Y. W.; Kim, M.; Kim, Z. H.; Han, S. W. *J. Am. Chem. Soc.* **2009**, *131*, 17036−17037.
(31) Wang, D.; Li, Y. *J. Am. Chem. Soc.* **2010**, *132*, 6280−6281.
(32) Wang, L.; Yamauchi, Y. *J. Am. Chem. Soc.* **2010**, *132*, 13636−13638.
(33) Ortiz, N.; Weiner, R. G.; Skrabalak, S. E. *ACS Nano* **2014**, *8*, 12461−12467.
(34) Wang, Y.; Peng, H.-C.; Liu, J.; Huang, C. Z.; Xia, Y. *Nano Lett.* **2015**, *15*, 1445−1450.
(35) Peng, H.-C.; Park, J.; Zhang, L.; Xia, Y. *J. Am. Chem. Soc.* **2015**, *137*, 6643−6652.
(36) Zhang, H.; Jin, M.; Wang, J.; Li, W.; Camargo, P. H.; Kim, M. J.; Yang, D.; Xie, Z.; Xia, Y. *J. Am. Chem. Soc.* **2011**, *133*, 6078−6089.
(37) Huang, X.; Li, Y.; Li, Y.; Zhou, H.; Duan, X.; Huang, Y. *Nano Lett.* **2012**, *12*, 4265−4270.
(38) Luty-Błocho, M.; Pacławski, K.; Wojnicki, M.; Fitzner, K. *Inorg. Chim. Acta* **2013**, *395*, 189−196.
(39) Feldberg, S.; Klotz, P.; Newman, L. *Inorg. Chem.* **1972**, *11*, 2860−2865.
(40) Timoshkin, A. Y.; Kudrev, A. G. *Russ. J. Inorg. Chem.* **2012**, *57*, 1362−1370.
(41) Kitchin, J. R.; Nørskov, J. K.; Barteau, M. A.; Chen, J. G. *Phys. Rev. Lett.* **2004**, *93*, 156801−156804.
(42) Wang, J. X.; Inada, H.; Wu, L.; Zhu, Y.; Choi, Y.; Liu, P.; Zhou, W.-P.; Adzic, R. R. *J. Am. Chem. Soc.* **2009**, *131*, 17298−17302.
(43) Wang, X.; Orikasa, Y.; Takesue, Y.; Inoue, H.; Nakamura, M.; Minato, T.; Hoshi, N.; Uchimoto, Y. *J. Am. Chem. Soc.* **2013**, *135*, 5938−5941.
(44) Mavrikakis, M.; Hammer, B.; Nørskov, J. K. *Phys. Rev. Lett.* **1998**, *81*, 2819−2822.
(45) Wu, J.; Li, P.; Pan, Y.-T.; Warren, S.; Yin, X.; Yang, H. *Chem. Soc. Rev.* **2012**, *41*, 8066−8074.
(46) Wang, X.; Vara, M.; Luo, M.; Huang, H.; Ruditskiy, A.; Park, J.; Bao, S.; Liu, J.; Howe, J.; Chi, M.; Xie, Z.; Xia, Y. *J. Am. Chem. Soc.* **2015**, *137*, 15036−15042.